

Article

Experimental Validation of a Numerical Coupling Environment Applying FEM and CFD †

Christopher Hartmann ^{1,*} , Julia Schweikert ¹, François Cottier ², Ute Israel ², Jochen Gier ² and Jens von Wolfersdorf ¹

¹ Institute of Aerospace Thermodynamics (ITLR), University of Stuttgart, Pfaffenwaldring 31, 70569 Stuttgart, Germany; julia.schweikert@itlr.uni-stuttgart.de (J.S.); jens.vonwolfersdorf@itlr.uni-stuttgart.de (J.v.W.)

² MTU Aero Engines AG, Dachauer Strasse 665, 80995 München, Germany; francois.cottier@mtu.de (F.C.); ute.israel@mtu.de (U.I.); jochen.gier@mtu.de (J.G.)

* Correspondence: christopher.hartmann@itlr.uni-stuttgart.de

† This paper is an extended version of our meeting paper published in the 15th European Turbomachinery Conference, Budapest, Hungary, 24–28 April 2023.

Abstract: Experimental results for the transient heat transfer characteristics over a flat plate and over a plate with V-shaped ribs were compared to numerical results from a coupling environment applying FEM and CFD. In order to simulate transient effects in the cooling process of engine components during typical flight missions, the temperature and the velocity at the inlet of the channel were varied over time. The transient temperature distribution at the plate was measured using infrared thermography. Five different plate materials (perspex, PEEK, quartz, aluminum, and steel) were considered to investigate the influence of thermal conduction on the heat transfer between solid and fluid depending on the Biot number. The experimental results represent a reference database for a Python-based coupling environment applying CalculiX (FEM) and ANSYS CFX (CFD). The results were additionally compared to numerical results simulating the complete transient conjugated heat transfer with CFD. A good agreement between the numerical and the experimental results was achieved using different coupling sizes at different Biot numbers for the flat plate and the plate with V-shaped ribs.

Keywords: transient; conjugate; heat-transfer; IRT; coupling; CHT



Citation: Hartmann, C.; Schweikert, J.; Cottier, F.; Israel, U.; Gier, J.; von Wolfersdorf, J. Experimental Validation of a Numerical Coupling Environment Applying FEM and CFD. *Int. J. Turbomach. Propuls. Power* **2023**, *8*, 31. <https://doi.org/10.3390/ijtp8030031>

Academic Editor: Michel Dumas

Received: 20 June 2023

Revised: 25 June 2023

Accepted: 29 August 2023

Published: 4 September 2023



Copyright: © 2023 by the authors. Licensee MDPI, Basel, Switzerland. This article is an open access article distributed under the terms and conditions of the Creative Commons Attribution (CC BY-NC-ND) license (<https://creativecommons.org/licenses/by-nc-nd/4.0/>).

1. Introduction

An essential task in the development process of modern aero engines is designated to the cooling mechanisms of the thermally high-stressed engine components. The component life—and, consequently, that of the entire engine—depends strongly on the material temperatures and requires, therefore, reliable prediction of the material temperatures for typical flight missions. Conjugate heat transfer (CHT), first formulated by Perelman [1], considers the interaction between solid and fluid. The flow conditions strongly influence the material temperatures and thermal interactions. Thus, secondary flows occur in cavities in compressors and turbines. For optimum design, transient processes and solid–fluid interaction, as well as the thermal time disparity for the solid and fluid, have to be considered. Transient analyses of temperature and stress distributions in turbine components usually use the finite element method. The occurring thermal loads are described by simplified boundary condition models from empirical correlations using advective one-dimensional models, as presented by Fiedler et al. [2]. Heselhaus and Vogel [3] have shown that, through transient, conjugate-flow, and heat-transfer simulations that take three-dimensional effects into account, a significant improvement in accuracy can be achieved without relying on empirical correlations. Thus, the prediction of component temperatures can be significantly improved, as Felippa et al. [4] have shown. Inappropriate modeling of the transient effects

during flight changes can lead, in contrast, to critical clearances or thermal stress, like Sun et al. [5] and Amirante et al. [6] have reported. Thermal time disparities make conjugated heat transfer simulations of a complete mission considering all time scales extremely expensive because convective heat transfer in the fluid is up to 10^4 times faster than the solid heat conduction, which was reported by He and Oldfield [7].

In order to reduce the computational effort, Errera and Baqué [8] and Sun et al. [5] introduced coupled aerothermomechanical methods, where optimized programs are used to independently simulate the heat transfer in the fluid and solid. This so-called weak coupling makes it possible to calculate the thermal behavior of the solid using an FEM code, whereas the adjacent flow is calculated by means of CFD. In order to ensure a physical, accurate, and stable solution for the conjugate system, the FEM and CFD codes need to exchange information at their common interface. For this different strategies exist in the literature. Errera and Duchaine [9] investigated different coupling coefficients and the continuity of exchange variables for aerothermal simulations. They showed that, if a criterion based on the ratio of thermal resistances at the interface is met, the Dirichlet–Robin transmission procedure leads to stable and fast convergence. Gimenez et al. [10], Houry et al. [11], and Moretti et al. [12]) presented approaches updating boundary conditions between coupling points. They showed that a quasi-dynamic coupling method with transient calculations for the solids and steady fluid calculations is the most promising in terms of accuracy and efficiency. Further, Gimenez et al. [10] demonstrated that a relaxation parameter value close to the heat transfer coefficient is beneficial. For conjugate heat transfer problems, the Biot number is a key parameter for the stability of the coupling scheme, as Verstraete and Scholl [13] identified.

Sun et al. [14] evaluated the applicability of such an approach for operating point changes in a low-pressure turbine cavity, Verdicchio et al. [15] for turbine discs, Dixon et al. [16] for main annulus gas path interactions, and Ganine et al. [17] for an internal air system with multiple cavities. Errera and Baqué [8] used this approach to investigate transient heat conduction in a flat plate subjected to a time-varying flow. For this particular case, computational time saving of up to 90% compared to strong coupling was documented with good accuracy.

In this context, an external Python-based coupling interface has been developed at the Institute of Aerospace Thermodynamics (ITLR) by Schindler et al. [18]. The interface couples the open-source FEM code CalculiX introduced by Dhondt [19] in transient mode with a steady-state CFD simulation for the fluid. For the present study, the commercial CFD software ANSYS CFX was used. In order to qualify the coupling interface, a reference database was generated using transient measurements. The experimental setup involved a channel flow over a flat plate, as well as an arrangement of five periodic V-ribs. Whereas most test facilities allow the regulation of just one boundary condition, the present setup allowed the independent setting of time-variable temperature and velocity inlet conditions. With simultaneous spatial and temporal high-resolution IRT, the wall temperature can be measured and the wall heat flux at the solid–fluid interface can be calculated with the semi-analytical approach described by Estorf [20]. Thereby, a reference dataset with which the coupling environment can be stressed in terms of different parameters can be generated where changes in the boundary conditions as they may occur in real applications are considered. Israel et al. [21] showed the applicability of the presented coupling environment for industry-related uses.

The aim of this study was to generate and demonstrate the capabilities of the experimental facility as validation for both CHT simulations and a coupling environment with different Biot numbers, different geometries, and different time-dependent inlet boundary conditions as an extended version of Hartmann et al [22].

2. Experimental Setup

An experimental test facility for local time-resolved transient heat transfer measurements has been designed by Liu et al. [23]. Brack et al. [24] modified the basic setup

to investigate unsteady convective heat transfer under controlled airflow velocity and temperature variation.

For the present work, the test rig was adapted to measure time-resolved transient heat transfer phenomena for different materials and turbulator geometries under generic and industry-related operating conditions. The experimental setup is shown in Figure 1. A vacuum pump was used to suck air from the ambient environment through a dust filter. The air is heated by a mesh heater and enters a test section with a constant cross-section of $0.12\text{ m} \times 0.15\text{ m}$. The time-variable temperature and velocity at the inlet of the channel can be set independently using a LabVIEW routine, which adjusts the power of the electrical mesh heaters and the positioning of the rotating vanes at the end of the channel (see Brack et al. [24]). With two hot-wire anemometers from SVMtec, the inlet boundary conditions were monitored, with one working in constant current mode to measure the inlet temperature (CCT) and the other in constant temperature mode to measure the inlet velocity (CTA). Both were located 0.205 m upstream of the flat plate. The plate with the dimensions $0.92\text{ m} \times 0.12\text{ m} \times 0.03\text{ m}$ was positioned in the center of the channel, dividing the test section into two subchannels. A trip wire at the beginning of the flat plate ensures a turbulent flow. On the top of the test section, a 5 mm thick CaF_2 window was installed to offer optical access for the IRT camera, an FLIR SC7600, which measured the surface radiation in a spectral range from $1.5\text{ }\mu\text{m}$ to $5.1\text{ }\mu\text{m}$ at 25 Hz . To ensure constant and equal emittance, the test plate was sprayed with a black paint (type SPB100 from Hallcrest). For in situ calibration of the IRT data, two surface thermocouples were inserted into the plate to measure the surface temperature.

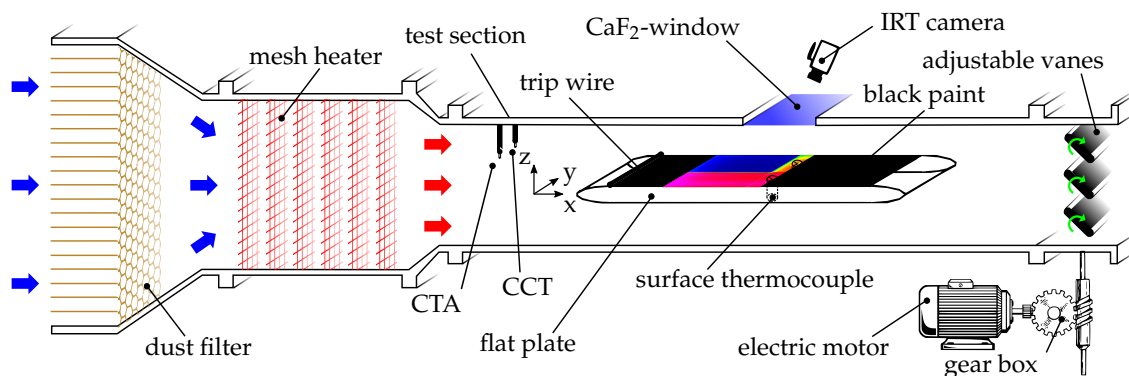


Figure 1. Experimental setup.

For the baseline configuration, the flat plate was made from perspex. In order to investigate the influence of heat conduction to convection between the solid and fluid, the material of the plate was varied in one section with the dimensions $0.25\text{ m} \times 0.06\text{ m} \times 0.015\text{ m}$. As visualized in Figure 2a, the material was changed using two inlays, with one always being made from perspex to ensure repeatability. The field of view (FOV) of the IRT camera started from 110 mm behind the beginning of the inlays and included the thermocouples for in situ calibration. Besides the flat plate, a plate with five V-shaped ribs was further investigated, which can be seen in Figure 2b. The 90° squared ribs with dimensions $e = 10\text{ mm}$ were glued on the test plate with a pitch of $p = 0.1\text{ m}$, resulting in two visible ribs for the IRT camera. Both geometries were investigated in five different test cases, which are shown in Figure 3. First, generic test cases were investigated, including a temperature jump (jump), a temperature ramp (ramp A) with constant velocity, and a velocity ramp (ramp B) with constant temperature. Afterwards, two transient cycles were investigated. One was typical for a flight mission, with opposite changes in temperature and velocity (cycle A), and one used an inversion in the heat flux to amplify the conjugate situation (cycle B).

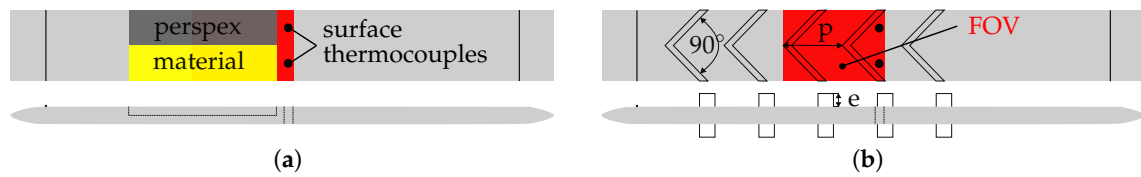


Figure 2. Test geometries: (a) flat plate, (b) plate with V-shaped ribs.

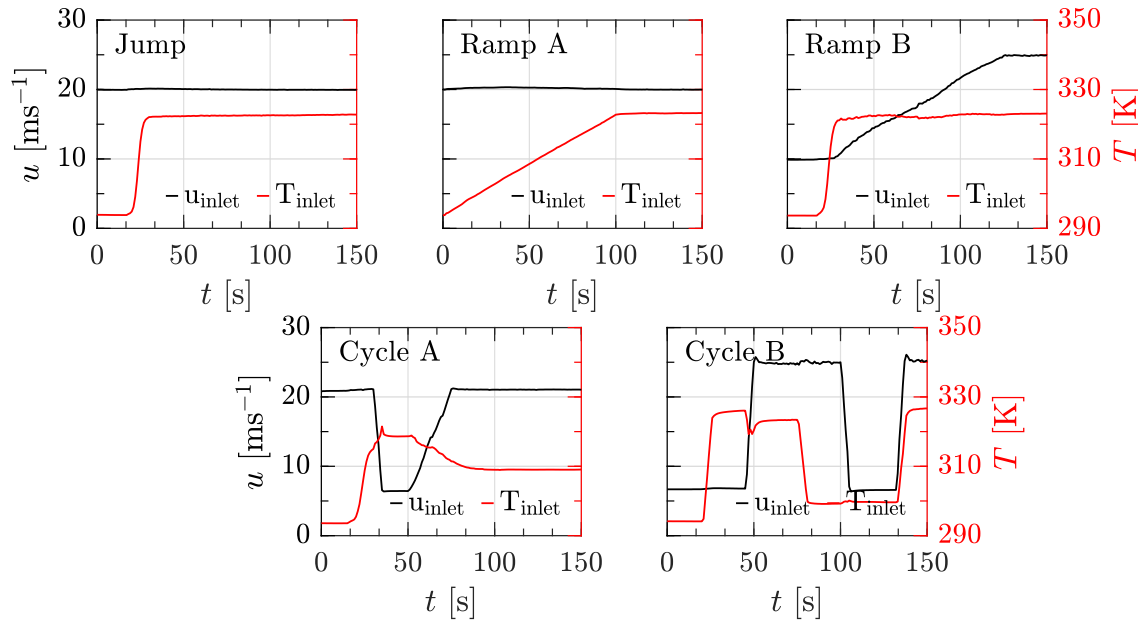


Figure 3. Boundary conditions.

3. Numerical Setup

The numerical setup consisted of one part of the channel, including the complete test plate, as is shown in Figure 4a. The inlet to the fluid domain was located 0.25 m upstream of the plate. The outlet was positioned 0.25 m downstream of the plate. Only one half of the channel height was simulated, using a symmetry condition at $z = 0$. The flat plate divided the channel height (0.15 m) into two sub-channels, each 0.06 m high. This resulted in an aspect ratio of 2:1 for each sub-channel. Due to the absence of lateral flow effects in the case of the flat plate, sidewalls and the lateral effects were negligible, and a 2D setup was simulated. To further validate this, a 3D setup for the flat plate case was investigated in a pre-test, showing negligible differences in the results. For the case with five V-ribs, a 3D setup was used. The fluid domain was discretized with a block-structured C- or H-grid in ANSYS ICEM 20.2. The dimensionless distance of the first node near the wall lay within $y_1^+ < 1$. For the ribbed geometry, the region directly behind and in front of the ribs was finely meshed with a C-shaped grid to guarantee the required near-wall resolution and to consider boundary layer effects. For the CHT simulations in the fully implicit, coupled multigrid solver ANSYS CFX, the solid domain was discretized with a block-structured grid in ANSYS ICEM, resulting in an 1:1 mesh connection at the interface. For the coupling with CalculiX, the solid domain consisted of four-node tetrahedral elements, as shown in Figure 4b, while the fluid mesh was identical. The data transfer between the two meshes used for the coupling environment was undertaken by transforming the respective grid into a universal format. There, each data point was assigned to a Cartesian point. The mapping between the two grids was then undertaken using the griddata function and a nearest-neighbor interpolation algorithm.

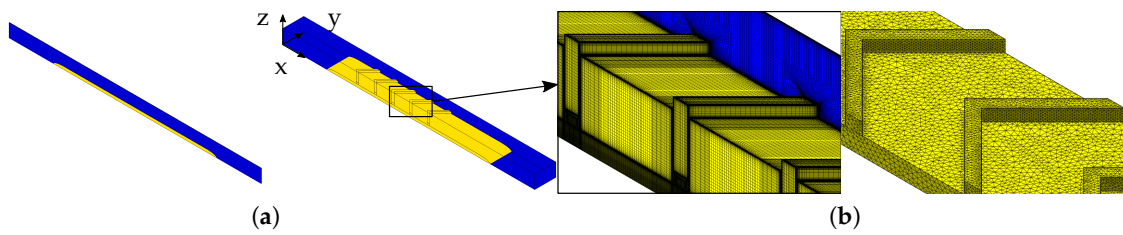


Figure 4. Numerical setup: (a) flat plate (left) and V-shaped ribs (right). (b) CFX (left) and CCX (right) mesh.

To solve the unsteady Reynolds-averaged Navier–Stokes equations, the SST turbulence model developed by Menter [25] was used, which provides a good compromise between high accuracy and acceptable computation time. For the rib geometry, reattachment modification and curvature correction were enabled, as the standard SST model tends to overpredict the separation region of a detached flow (see Menter et al. [26]). The advection terms were discretized with the default quasi-second-order discretization scheme in CFX, which is called High Resolution. The transient terms were discretized with a second-order backward Euler scheme, while the convergence criteria were of a root-mean-square type for the conservation equations targeted to be 10^{-7} . The modified setup has shown good results in comparable complex cooling channels (see Göhring et al. [27]). At the inlet, the transient boundary conditions of the temperature and velocity were taken according to the hot-wire measurements. At the outlet, a constant pressure was imposed as an averaged value from the experiment. For the CHT simulations, a time-step size of $t_{\text{CHT}} = 1$ s was used to simulate the whole experimental duration of $t_{\text{total}} = 150$ s. Even though the time-step size was relatively large, a stable solution was achieved, and the results from the monolithic approach were intended to function as a reference for the coupling. The channel walls were set as adiabatic and the fluid was modeled as an ideal gas. Dynamic viscosity η and thermal conductivity k , were modeled as temperature-dependent using the formula presented by Sutherland [28] with the coefficients presented by White [29]. The material quantities for the respective solid domain, which were taken from the manufacturers, are summarized in Table 1.

Table 1. Material quantities.

	Perspex	PEEK	Quartz	Steel	Aluminum
ρ [kg m ⁻³]	1190	1310	2200	7900	2700
c_p [J kg ⁻¹ K ⁻¹]	1470	1340	670	500	888
k [W m ⁻¹ K ⁻¹]	0.19	0.25	1.4	15	237

4. Coupling Environment

The coupling environment, developed by Schindler et al. [18], controls the communication between the thermal FEM solver CalculiX for the solid domain and a user-defined FVM solver for the fluid domain. For the present study, the commercial solver ANSYS CFX V21.1 was used, which is a common tool for industrial applications (Cottier et al. [30]).

With the Python-based coupling environment, the transient effects inside the solid were simulated using CalculiX. This yielded the spatially and temporally resolved temperature evolution in the structure. By means of steady-state CFD simulations at selected times, thermal feedback, flow, and an interface update were enabled. The procedure of the coupling algorithm is demonstrated in Figure 5. After initialization of both codes (1), CalculiX ran in transient mode with a time interval of $\Delta t_{\text{ccx}} = 0.2$ s (2) until the coupling time interval t_{cpl} was reached. In the course of this, a Robin condition ($q_{\text{solid}}^v(t) = h^v(t)(T_{\text{solid}}^v(t) - T_{\text{ref}}^v(t))$) was imposed on the solid-side interface. For the first subiteration $v = 1$, a constant T_{ref}^v and h^v based on t_{i-1} was used. At each coupling point,

the FEA results were then imposed as a Dirichlet condition on the fluid side for the steady CFD ($T_{\text{fluid}}^v(t_i) = T_{\text{solid}}^v(t_i)$). Thus, a combination of Dirichlet and Robin conditions to exchange T_{ref} or h (via \dot{q}), respectively, at the interface between adjacent fluid and solid domains was used (3). Using a root-mean-square evaluation of $T_{\text{fluid}}^v - T_{\text{fluid}}^{v-1}$ at the interface for all points at the interface, convergence was checked (4). If no convergence was reached, T_{ref} and h were updated with a linear interpolation from the converged values of the old coupling step at t_{i-1} (5). Then, CalculiX was run with the updated transient Robin condition. This was repeated until $\epsilon < \epsilon_{\text{max}}$ or the maximum number of subiterations ν was reached (6). Thereby, the coupling interval depended on the variation of the boundary conditions. To additionally accelerate convergence, a relaxation method proposed by Aitken [31] was implemented.

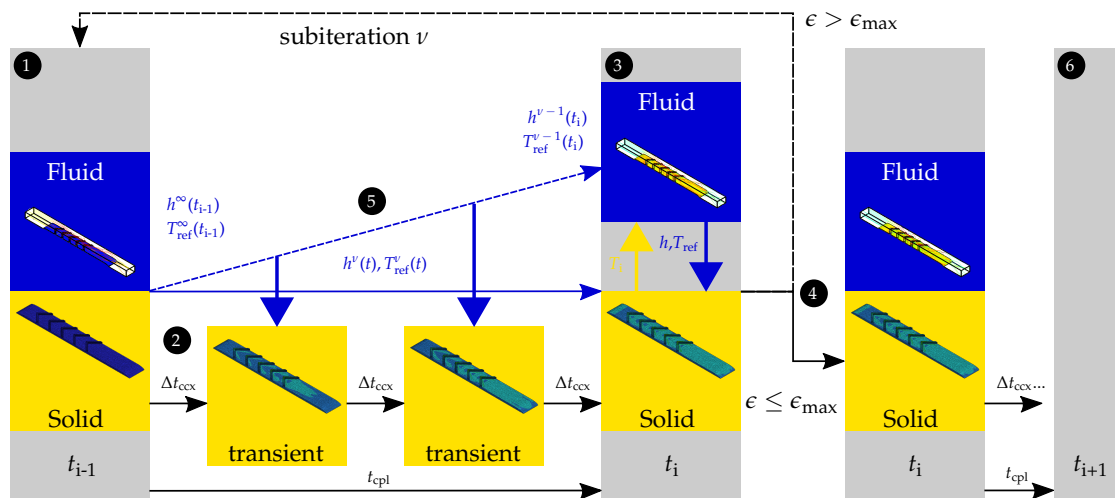


Figure 5. Coupling scheme.

An overview of the studied geometries, numerical approaches, test cases, and investigated materials is given in Table 2.

Table 2. Overview of the studied geometries, approaches, cases and materials.

Geometry	Approach			Test Case				Material					
	E x p	C H T	C p l	Jump	Ramp		Cycle		Perspex	PEEK	Quartz	Aluminium	Steel
					A	B	A	B					
Flat plate	X	X	X	X	X	X	X	X	X	X	X	X	X
V-ribs	X	X	X	X	X	X	X	X	X				

5. Data Reduction and Evaluation

Using the two hot-wire anemometers at the channel inlet, the boundary conditions T_{inlet} and u_{inlet} were measured with a frequency of 4000 Hz. The wall temperature T_w was temporally and spatially resolved with a frequency of 25 Hz and a spatial resolution of 0.4 mm/pixel for $t_{\text{exp}} = 150$ s. The data were filtered by means of a 3D Gaussian filter and, for better handling, the frequency for all measurements was afterwards reduced to 5 Hz. Even with a frequency of 5 Hz, it was ensured that the step changes in the boundary conditions (see Figure 3), which always occur within 5 s, could be sufficiently resolved and did not affect the results. To evaluate the temporally and spatially resolved wall heat flux \dot{q}_w , a method developed by Estorf [20] was used. The method ensures the equality of the heat flux into the solid and of the fluid. It is based on the analytical solution of the transient heat transfer equation within the wall for constant material properties and considers 3D

lateral heat conduction effects by taking into account the transient surface temperature of an area surrounding each evaluation point within the infrared image. For the validity of the method, isothermal initial conditions for the whole experimental setup have to be ensured. So, the plate was at ambient temperature at the beginning of each experiment and was subsequently heated up by a time-dependent hot flow. Second, the wall has to be semi-infinite, limiting the experiment duration to

$$t_{\infty} = \frac{\rho c_p L^2}{k} \frac{1}{4} \quad (1)$$

as indicated by Vogel and Weigand [32]. This criterion ensures a deviation from the analytical solution for an adiabatic backside of less than 2% (cf. Wagner et al. [33]). For the investigated materials given in Table 1, this resulted in valid evaluation times for the wall heat flux from less than 1 s for aluminum to over 500 s for perspex (see Table 3). With T_w , \dot{q}_w , and the inlet temperature as the reference temperature of the fluid ($T_{\text{ref}} = T_{\text{inlet}}$), the wall heat transfer coefficient h_w can be calculated using Newton's law of cooling:

$$h_w = \frac{\dot{q}_w}{T_w - T_{\text{ref}}}. \quad (2)$$

To investigate the influence of thermal conduction on the heat transfer between solid and fluid, the Biot number,

$$Bi = \frac{hL}{k}, \quad (3)$$

was varied. With a typical heat transfer coefficient for a flat plate at the given flow velocities of $60 \text{ W m}^{-2} \text{ K}^{-1}$ (cf. Kays et al. [34]) and a characteristic length of $L = 0.015 \text{ m}$, a wide range of Biot numbers could be investigated with the chosen materials (see Table 3).

Table 3. Time for semi-infinite evaluation and Biot numbers for investigated materials.

	Perspex	PEEK	Quartz	Steel	Aluminum
t_{∞} (s)	517.9	395.0	59.2	14.8	0.6
Bi ($h_w = 60 \text{ W m}^{-2} \text{ K}^{-1}$)	4.7	3.6	0.64	0.06	0.0038

The measured quantities T_{inlet} , u_{inlet} , and T_w , as well as the evaluated ones, \dot{q}_w and h_w , were subject to uncertainties. The hot-wire probes were calibrated directly by the manufacturer to 0.1 ms^{-1} (CTA) or in situ to 0.1 K (CCT). The surface thermocouples were calibrated with a dry block calibrator (AMETEK RTC-159B) to an uncertainty of 0.1 K . Based on the method described by Moffat [35], the relative uncertainties for $\delta\dot{q}_w/\dot{q}$ and $\delta h_w/h_w$ vary between 10% and 15% depending on the mission, evaluation position, and time (see Brack et al. [24] for details). Figure 6 shows the field of view of the IRT camera, including the positions for the final evaluation for the flat plate and the ribbed geometry.

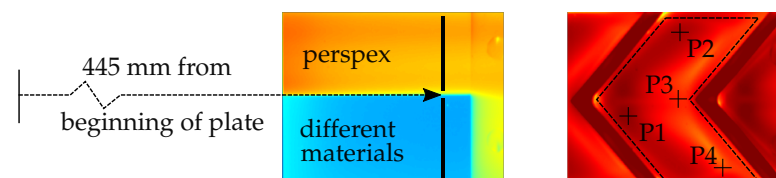


Figure 6. Positions for final evaluation.

The method used by Estorf [20] to calculate heat flux was derived for rectangular adiabatic edges. In order to minimize the uncertainties of the method near the edges, for the flat plate, the results were averaged in the lateral direction at $x = 445 \text{ mm}$, neglecting the near wall region and the region near the interface between the different material inlays.

For the ribbed geometry, the surface between the two visible ribs was considered. Within this context, the evaluations were performed with four selected pixels.

6. Results

In the first step, a comparison of the experimental and numerical results for the flat plate with different materials was undertaken. In terms of validation, the coupling step was set constant with $t_{\text{cpl}} = 1$ s. The coupling step was afterwards varied over time, depending on the inlet boundary conditions for the perspex plate. Subsequently, the findings were transferred to the ribbed geometry, where the flow and heat transfer characteristics were more complex.

6.1. Flat Plate

For the validation of the coupling environment, the results from the FEM and CFD were coupled every $t_{\text{cpl}} = 1$ s. The physical time-step size in the CHT simulations was set to $t_{\text{CHT}} = 1$ s to accordingly model the transient effects in the coupling. A further reduction of t_{CHT} showed no effect on the transient behavior. In Figure 7, the resulting local wall temperature distributions for the investigated inlet conditions shown in Figure 3 are plotted. The solid line with the star symbols shows the experimental results. The dashed line describes the CHT solution and the dashed and dotted line the coupling environment. The different materials are shown in different colors. Since the tests were carried out on different days, the ambient temperature at the beginning of the tests was not exactly identical, but this was taken into account in the numerical simulations. The numerical results for T_w were in good accordance with the experimental data for all investigated inlet conditions and materials. This shows that, with the chosen time-step size, the transient heat transfer characteristics at the interface could be captured. Between the numerical simulations (CHT and coupling), no differences were visible for either of the cases. Even for materials with low Biot numbers, like steel and aluminum, the numerical values fit the experimental ones accurately.

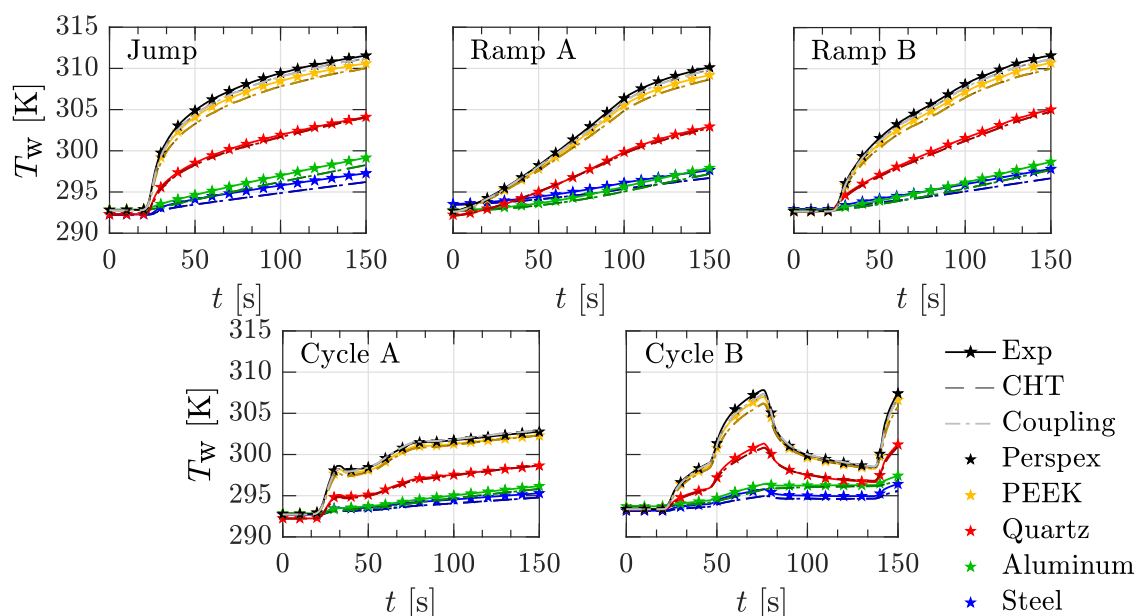


Figure 7. Transient wall temperature at $x = 455$ mm for the flat plate with different materials.

The corresponding \dot{q}_w is given in Figure 8. The overall agreement between the experiment and the numerical simulations was good and the numerical data were identical. For the experimental evaluation of the wall heat flux, the method described by Estorf [20] showed good agreement for all investigated materials, as long as its assumptions were valid. As the semi-infinite wall assumption was not valid for steel and aluminum (see Table 3),

no experimental results are shown. According to Vogel and Weigand [32], the limit for quartz is reached 60 s after a heat flux is imposed. For the generic cases, this resulted in diverging heat fluxes shown by experimental and numerical values 60 s after the initial temperature jump, which corresponded to 85 s from the start. As the driving temperature difference for cycle A was lower, the deviations were less pronounced. For cycle B, it was visible that, even for a negative heat flux, the semi-infinite wall assumption time was not extended and the agreement between the experiment and numerical simulations remained. As the Biot number is a typical definition used to characterize conjugate thermal systems, it can be summarized that the coupling environment stability was proven with a wide range of Biot numbers and validated by experimental data with a generic character, as well as for transient cycles.

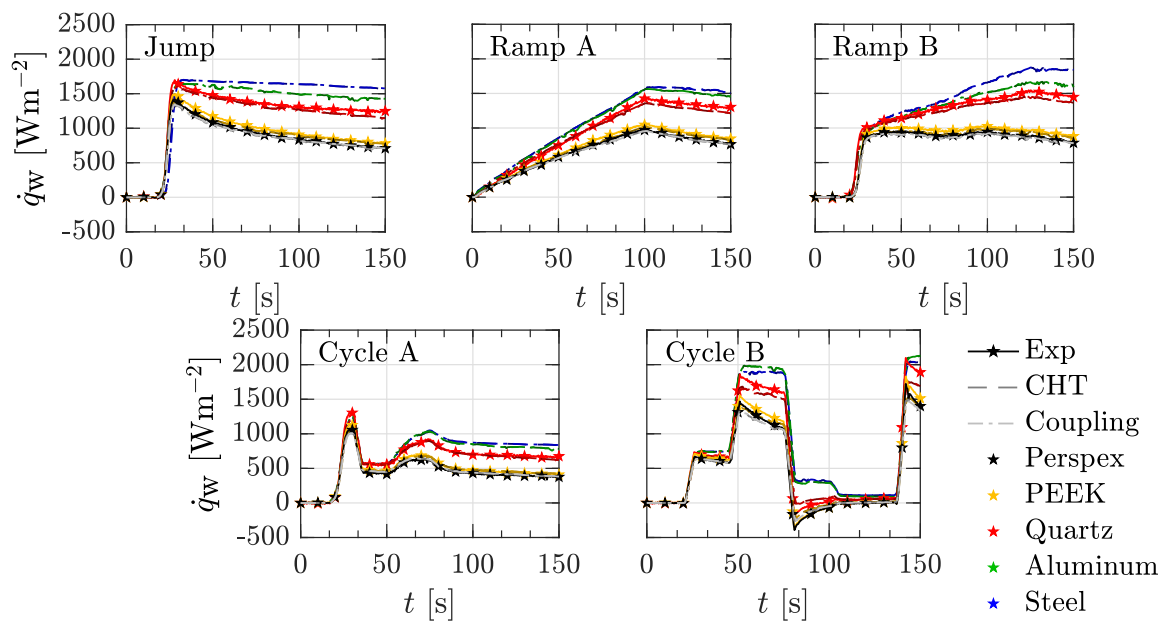


Figure 8. Transient wall heat flux at $x = 455$ mm for the flat plate with different materials.

In order to reduce the computational time, the coupling environment provides the opportunity to couple the FEM and CFD only at specific coupling points. In this respect, a coupling point was set at every step change in the inlet boundary conditions. To evaluate the quality of the coupling scheme, only the results for perspex are discussed. In Figure 9, the experimental values of T_w and \dot{q}_w , as well as the numerical ones, from the coupling with variable coupling sizes are shown. The coupling points are marked with the dots.

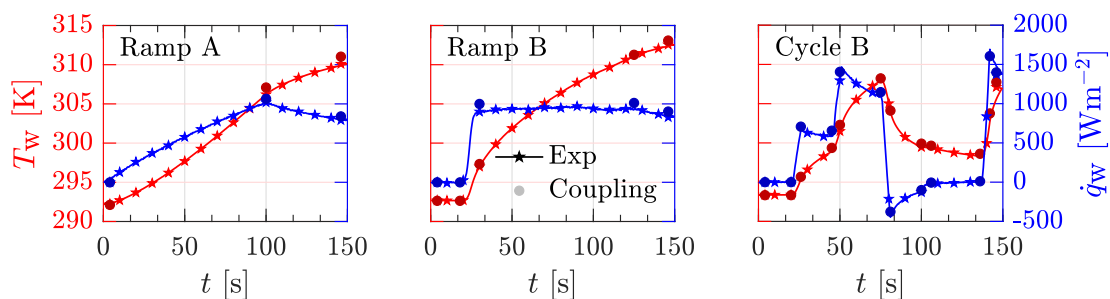


Figure 9. Transient wall temperature and transient wall heat flux at $x = 455$ mm for the flat plate with variable coupling sizes for different test cases.

For all test cases, the numerical simulation showed good agreement with the experimental results. In comparison to a constant coupling time step of $t_{cp1} = 1$ s, the simulation time was reduced to 10% or less. In summary, the coupling environment with its inner

subiterations and linear changing of the boundary conditions was validated for different materials with variable coupling sizes for linear changing inlet boundary conditions at the flat plate.

6.2. Plate with V-Shaped Ribs

In order to obtain a deeper understanding of the heat transfer phenomena, the local wall temperatures for two ribs from the CHT and experiment are plotted in Figure 10a at $t = 50$ s. The overall agreement was good, but in the numerical results, the region with the highest temperatures in the reattachment zone was slightly shifted towards the upstream rib. The increase in heat transfer in the near-wall region was also overestimated compared to the experimental results. A comparison of the transient behavior of T_w and \dot{q}_w at four selected points is given in Figure 10b for cycle A. The overall agreement was fair. Compared to the experiment, larger deviation in the temperature and heat flux for P4 occurred, whereas the differences between the numerical data were negligible.

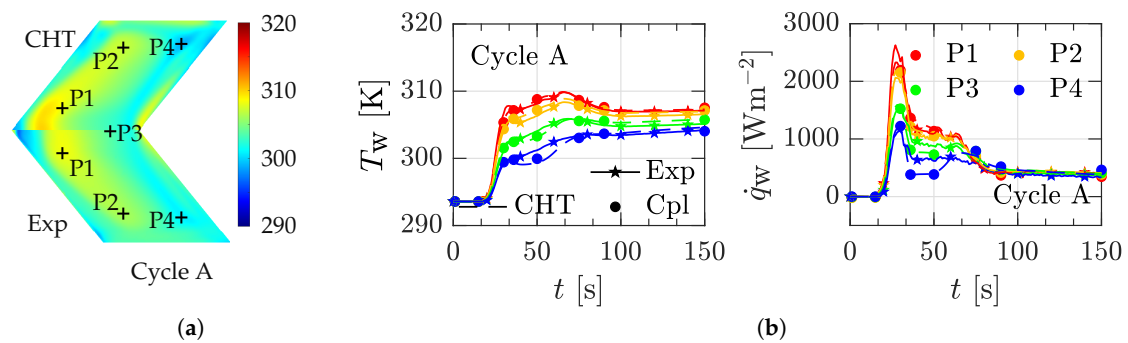


Figure 10. Comparison of experimental and numerical results for the V-shaped ribs: (a) surface plot at $t = 50$ s; (b) wall heat temperature (left) and wall heat flux (right).

To investigate this further, the heat transfer coefficient for the experiment and CHT is shown in Figure 11a. At the beginning of the experiment, T_w equaled T_{ref} , so the heat transfer coefficient was not defined. It varied with the change in velocity at the inlet, and the deviation between the experiment and CHT was more pronounced in the low-velocity region (see Figure 3). Figure 11b shows the ratio of the heat transfer coefficients of the experiment and CHT for cycle A and the jump. While it remained constant around unity for the jump, h_w at low velocities was partly overestimated by the numerical data. A reason for this could have been an incorrect prediction for the entropy generation in the turbulence model. Due to the complex flow situation, different probe locations can be differently influenced by viscous effects, so dissipation depending on the local flow structures can be influenced by vortices. Probe P4, in particular, was in an area with unsteady and unstable vortices combined with flow separation before the next rib, whereas for P3, where the flow structures were relatively stable, the SST turbulence models showed good results compared to the experiment. According to Esfahani and Jafarian [36], for low velocities, the thermal component of entropy generation dominates over the frictional component in the boundary layer and has a large contribution, especially at the wall. This also introduces changes in local dissipation, which are not well accounted for in the numerical model, regardless of the CHT or coupled simulations, and leads to difficulties in predicting the correct flow and heat transfer characteristics with the used SST model (see Herwig [37]). After $t = 75$ s, h_w was less reliable due to the small differences in T_w and T_{ref} for cycle A, which explains the deviations in Figure 11b.

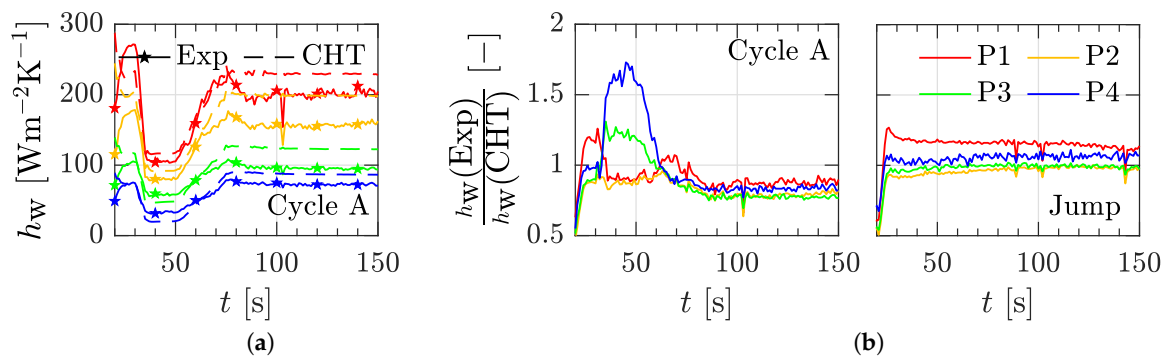


Figure 11. Transient wall heat transfer coefficient for different test cases: (a) transient h_w for cycle A; (b) ratio of experimental and numerical heat transfer coefficients for cycle A (left) and the jump (right).

However, the idea of linear ramping of boundary conditions between coupling points worked for all evaluation points with moderate changes in inlet boundary conditions, as shown in Figure 12 for different test cases using coupling points. The coupling points were again set at each step change in the inlet boundary conditions. The overall agreement for all evaluation points and test cases was fair, even for long coupling times of $t_{\text{cpl}} = 120$ s (jump), linear velocity changes (ramp B), and opposite changes in boundary conditions (cycle B).

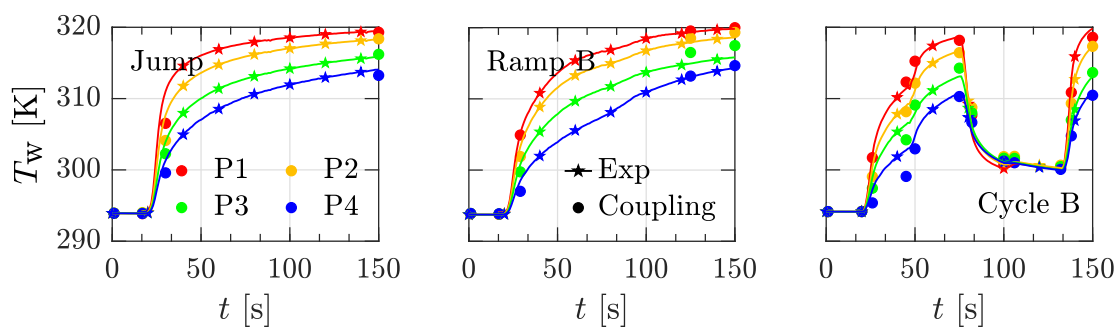


Figure 12. Transient wall temperature for different test cases using coupling points.

7. Conclusions

An experimental test rig for transient conjugate heat transfer measurements using IRT was presented in order to validate numerical simulations with a coupling environment for different Biot numbers. A channel flow over a flat plate and a plate with V-shaped ribs was investigated. The linear approach to efficiently couple the transient FEM code and steady-state FVM solver was successfully demonstrated. It was shown that the stability of the coupling process was guaranteed over a wide range of Biot numbers. For the comparison of experimental and numerical results, no significant differences were found for the flat plate. In the case of the V-shaped ribs, the numerical setup showed difficulties in the simulation of parts of the anisotropic turbulent effects. The overall agreement with the experimental results was still satisfying. With the coupling environment and its possibility of coupling the FEM and FVM only at defined points, the computational time can be extremely reduced while maintaining good temperature prediction. In the future, the described procedure can be extended to include multiple more complex independent boundary conditions through the introduction of transition curves. For modern aero engines, by using the transient temperature data of the FEM solver, structural analysis and stress calculation can be improved and the operational lifetime of thermally high-stressed engine components can be increased. Moreover, the results underline the capabilities of the experimental facility as validation for transient conjugated heat transfer phenomena.

Author Contributions: Conceptualization, C.H. and J.v.W.; methodology, C.H., J.S. and F.C.; software, C.H. and U.I.; validation, C.H. and F.C.; formal analysis, C.H.; investigation, C.H.; resources, J.v.W.; data curation, C.H. and F.C.; writing—original draft preparation, C.H.; writing—review and editing, J.S., F.C. and J.v.W.; visualization, C.H.; supervision, J.G. and J.v.W.; project administration, J.G. and J.v.W.; funding acquisition, J.v.W. All authors have read and agreed to the published version of the manuscript.

Funding: The investigations were conducted as part of the joint research program KuepLe in the frame of AG Turbo. The work was supported by the Federal Ministry for Economic Affairs and Climate Action (BMWK) as per the resolution of the German Federal Parliament under grant number 0324358I.

Institutional Review Board Statement: Not applicable.

Informed Consent Statement: Not applicable.

Data Availability Statement: Not applicable.

Acknowledgments: Not applicable.

Conflicts of Interest: Not applicable.

Nomenclature and Abbreviations

The following nomenclature is used in this manuscript:

Roman characters

c_p	specific heat capacity in $\text{J kg}^{-1} \text{K}^{-1}$
e	characteristic rib height in m
h	heat transfer coefficient in $\text{W m}^{-2} \text{K}^{-1}$
i	index
k	thermal conductivity in $\text{W m}^{-1} \text{K}^{-1}$
L	length in m
p	pitch of ribs in m
p	pressure in $\text{kg m}^{-1} \text{s}^{-2}$
\dot{q}	heat flux in W m^{-2}
t	time in s
T	temperature in K
u	velocity in m s^{-1}
x, y, z	coordinates in m
y^+	dimensionless wall distance

Greek characters

ϵ	norm
η	dynamic viscosity in $\text{kg m}^{-1} \text{s}^{-1}$
ν	subiteration number
ρ	density in kg m^{-3}

Subscripts

ccx	CalculiX
cpl	coupling
ref	reference
w	wall

The following abbreviations are used in this manuscript:

CCT	constant current thermometry
CFD	computational fluid dynamics
CHT	conjugate heat transfer
CTA	constant temperature anemometry
Exp	experiment
FEM	finite element method
FOV	field of view
FVM	finite volume method
IRT	infrared thermography
SST	shear stress transport

References

1. Perelman, T. On conjugated problems of heat transfer. *Int. J. Heat Mass Transf.* **1961**, *3*, 293–303. [[CrossRef](#)]
2. Fiedler, B.; Muller, Y.; Voigt, M.; Mailach, R. Comparison of Two Methods for the Sensitivity Analysis of a One-Dimensional Cooling Flow Network of a High-Pressure-Turbine Blade. In *Volume 2D: Turbomachinery*; American Society of Mechanical Engineers: New York, NY, USA, 2020. [[CrossRef](#)]
3. Heselhuis, A.; Vogel, D. Numerical simulation of turbine blade cooling with respect to blade heat conduction and inlet temperature profiles. In Proceedings of the 31st Joint Propulsion Conference and Exhibit, San Diego, CA, USA, 10–12 July 1995. [[CrossRef](#)]
4. Felippa, C.A.; Park, K.; Farhat, C. Partitioned analysis of coupled mechanical systems. *Comput. Methods Appl. Mech. Eng.* **2001**, *190*, 3247–3270. [[CrossRef](#)]
5. Sun, Z.; Chew, J.W.; Hills, N.J.; Lewis, L.; Mabilat, C. Coupled Aerothermomechanical Simulation for a Turbine Disk Through a Full Transient Cycle. *J. Turbomach.* **2011**, *134*, 011014. [[CrossRef](#)]
6. Amirante, D.; Hills, N.J.; Barnes, C.J. Thermo-Mechanical Finite Element Analysis/Computational Fluid Dynamics Coupling of an Interstage Seal Cavity Using Torsional Spring Analogy. *J. Turbomach.* **2012**, *134*, 051015. [[CrossRef](#)]
7. He, L.; Oldfield, M.L.G. Unsteady Conjugate Heat Transfer Modeling. *J. Turbomach.* **2010**, *133*, 031022. [[CrossRef](#)]
8. Errera, M.P.; Baqué, B. A quasi-dynamic procedure for coupled thermal simulations. *Int. J. Numer. Methods Fluids* **2013**, *72*, 1183–1206. [[CrossRef](#)]
9. Errera, M.P.; Duchaine, F. Comparative study of coupling coefficients in Dirichlet–Robin procedure for fluid–structure aerothermal simulations. *J. Comput. Phys.* **2016**, *312*, 218–234. [[CrossRef](#)]
10. Gimenez, G.; Errera, M.P.; Baillis, D.; Smith, Y.; Pardo, F. A coupling numerical methodology for weakly transient conjugate heat transfer problems. *Int. J. Heat Mass Transf.* **2016**, *97*, 975–989. [[CrossRef](#)]
11. Khoury, R.R.E.; Errera, M.P.; Khoury, K.E.; Nemer, M. Efficiency of coupling schemes for the treatment of steady state fluid–structure thermal interactions. *Int. J. Therm. Sci.* **2017**, *115*, 225–235. [[CrossRef](#)]
12. Moretti, R.; Errera, M.P.; Feyel, F. Temporal Interpolation Methods for Transient CHT. In Proceedings of the AIAA Scitech 2019 Forum, San Diego, CA, USA, 7–11 January 2019; American Institute of Aeronautics and Astronautics: Reston, VA, USA, 2019. [[CrossRef](#)]
13. Verstraete, T.; Scholl, S. Stability analysis of partitioned methods for predicting conjugate heat transfer. *Int. J. Heat Mass Transf.* **2016**, *101*, 852–869. [[CrossRef](#)]
14. Sun, Z.; Chew, J.; Hills, N.; Volkov, K.; Barnes, C. Efficient Finite Element Analysis/Computational Fluid Dynamics Thermal Coupling for Engineering Applications. *J. Turbomach.* **2010**, *132*, 031016. [[CrossRef](#)]
15. Verdicchio, J.A.; Chew, J.W.; Hills, N.J. Coupled Fluid/Solid Heat Transfer Computation for Turbine Discs. In *Volume 3: Heat Transfer; Electric Power; Industrial and Cogeneration*; American Society of Mechanical Engineers: New York, NY, USA, 2001. [[CrossRef](#)]
16. Dixon, J.A.; Valencia, A.G.; Coren, D.; Eastwood, D.; Long, C. Main Annulus Gas Path Interactions—Turbine Stator Well Heat Transfer. *J. Turbomach.* **2013**, *136*, 021010. [[CrossRef](#)]
17. Ganine, V.; Javiya, U.; Hills, N.; Chew, J. Coupled Fluid-Structure Transient Thermal Analysis of a Gas Turbine Internal Air System With Multiple Cavities. *J. Eng. Gas Turbines Power* **2012**, *134*, 102508. [[CrossRef](#)]
18. Schindler, A.P.; Brack, S.; von Wolfersdorf, J. Coupled FE-CFD analysis of transient conjugate heat transfer. In Proceedings of the 13th European Conference on Turbomachinery Fluid Dynamics and Thermodynamics, Lausanne, Switzerland, 8–12 April 2019. [[CrossRef](#)]
19. Dhondt, G. *The Finite Element Method for Three-Dimensional Thermomechanical Applications*; Wiley: Hoboken, NJ, USA, 2004.
20. Estorf, M. Image based heating rate calculation from thermographic data considering lateral heat conduction. *Int. J. Heat Mass Transf.* **2006**, *49*, 2545–2556. [[CrossRef](#)]
21. Israel, U.; Cottier, F.; Hartmann, C.; von Wolfersdorf, J. Method for transient and steady state partitioned fluid-structure interaction analysis in conjugate heat transfer for aero engines applications. In Proceedings of the 15th European Conference on Turbomachinery Fluid Dynamics and Thermodynamics, Budapest, Hungary, 24–28 April 2023. [[CrossRef](#)]
22. Hartmann, C.; Schweikert, J.; Cottier, F.; Israel, U.; Gier, J.; von Wolfersdorf, J. Experimental Validation of a Numerical Coupling Environment between FEM and CFD. In Proceedings of the 15th European Conference on Turbomachinery Fluid Dynamics and Thermodynamics, Budapest, Hungary, 24–28 April 2023. [[CrossRef](#)]
23. Liu, C.; von Wolfersdorf, J.; Zhai, Y. Time-resolved heat transfer characteristics for steady turbulent flow with step changing and periodically pulsating flow temperatures. *Int. J. Heat Mass Transf.* **2014**, *76*, 184–198. [[CrossRef](#)]
24. Brack, S.; Poser, R.; von Wolfersdorf, J. Experimental investigation of unsteady convective heat transfer under airflow velocity and temperature variations. *Meas. Sci. Technol.* **2021**, *33*, 015106. [[CrossRef](#)]
25. Menter, F.R. Two-equation eddy-viscosity turbulence models for engineering applications. *AIAA J.* **1994**, *32*, 1598–1605. [[CrossRef](#)]
26. Menter, F.R.; Kuntz, M.; Langtry, R. Ten years of industrial experience with the SST turbulence model. *Heat Mass Transf.* **2003**, *4*, 625–632.

27. Göhring, M.; Krille, T.; Feile, J.; von Wolfersdorf, J. Heat Transfer Predictions in Smooth and Ribbed Two-Pass Cooling Channels under Stationary and Rotating Conditions. In Proceedings of the 16th International Symposium on Transport Phenomena and Dynamics of Rotating Machinery, Honolulu, HI, USA, 10–15 April 2016. Available online: <https://hal.archives-ouvertes.fr/hal-01884254> (accessed on 13 April 2021).
28. Sutherland, W. LII. The viscosity of gases and molecular force. *Lond. Edinb. Dublin Philos. Mag. J. Sci.* **1893**, *36*, 507–531. [[CrossRef](#)]
29. White, F. *Viscous Fluid Flow*; McGraw-Hill Higher Education: New York, NY, USA, 2006.
30. Cottier, F.; Pinchaud, P.; Dumas, G. Aerothermal predictions of combustor/turbine interactions using advanced turbulence modeling. In Proceedings of the 13th European Conference on Turbomachinery Fluid Dynamics and Thermodynamics, Lausanne, Switzerland, 8–12 April 2019. [[CrossRef](#)]
31. Aitken, A.C. On Bernoulli's Numerical Solution of Algebraic Equations. *Proc. R. Soc. Edinb.* **1927**, *46*, 289–305. [[CrossRef](#)]
32. Vogel, G.; Weigand, B. A new evaluation method for transient liquid crystal experiments. In Proceedings of the 2001 National Heat Transfer Conference, ASME, Anaheim, CA, USA, 10–12 June 2001.
33. Wagner, G.; Kotulla, M.; Ott, P.; Weigand, B.; von Wolfersdorf, J. The Transient Liquid Crystal Technique: Influence of Surface Curvature and Finite Wall Thickness. *J. Turbomach.* **2005**, *127*, 175–182. [[CrossRef](#)]
34. Kays, W.; Crawford, M.; Weigand, B. *Convective Heat and Mass Transfer*; McGraw-Hill Series in Mechanical Engineering: New York, NY, USA, 2005; Volume 30.
35. Moffat, R.J. Contributions to the Theory of Single-Sample Uncertainty Analysis. *J. Fluids Eng.* **1982**, *104*, 250–258. [[CrossRef](#)]
36. Esfahani, J.A.; Jafarian, M.M. Entropy Generation Analysis of a Flat Plate Boundary Layer with Various Solution Methods. *Sci. Iran.* **2005**, *12*, 233–240.
37. Herwig, H. The Role of Entropy Generation in Momentum and Heat Transfer. *J. Heat Transf.* **2012**, *134*, 031003. [[CrossRef](#)]

Disclaimer/Publisher's Note: The statements, opinions and data contained in all publications are solely those of the individual author(s) and contributor(s) and not of MDPI and/or the editor(s). MDPI and/or the editor(s) disclaim responsibility for any injury to people or property resulting from any ideas, methods, instructions or products referred to in the content.